

# Achieving high capacity and long life of aqueous rechargeable zinc battery by using nanoporous-carbon-supported poly(1,5-naphthalenediamine) nanorods as cathode



Yi Zhao <sup>a</sup>, Yinong Wang <sup>b</sup>, Zhiming Zhao <sup>c</sup>, Jingwen Zhao <sup>c</sup>, Tuo Xin <sup>a</sup>, Na Wang <sup>a</sup>, Jinzhang Liu <sup>a,\*</sup>

<sup>a</sup> School of Materials Science and Engineering, Beihang University, Beijing, 100191, China

<sup>b</sup> Dalian University of Technology, Panjin, 124221, Liaoning Province, China

<sup>c</sup> Qingdao Institute of Bioenergy and Bioprocess Technology, Chinese Academy of Science, Qingdao, 266101, Shandong Province, China

## ARTICLE INFO

### Keywords:

Zn-ion battery  
Organic electrode material  
Aqueous battery  
Charge storage mechanism  
Nanoporous carbon

## ABSTRACT

Aqueous rechargeable Zn-ion batteries (ZIBs) are safe, low cost, and environmentally friendly, yet the realization of both high capacity and long cycling life remains a major challenge. Herein, electrodeposited poly(1,5-naphthalenediamine) nanorods over nanoporous carbon are used as the cathode material to make aqueous ZIBs that can be operated within the voltage range of 0.1 – 1.8 V and have merits of both ionic battery and supercapacitor. Flexible carbon fiber fabric and thick carbon fiber felt are used as current collectors, respectively, to support the polymer/carbon composite with different mass loadings. With using the carbon fabric, flat pouch cells and cable-shaped micro cells are fabricated and show stable electrochemical performances when repeatedly bent at large angles. The pouch cells show maximum energy and power densities of 195 Wh kg<sup>-1</sup> and 10<sup>4</sup> W kg<sup>-1</sup>, respectively, and achieve a capacity retention of 91% after 10000 cycles. The prototype cell with using a 3 mm-thick carbon felt shows higher energy densities up to 7.7 mWh cm<sup>-2</sup> and better cycling stability, i.e., 100% capacity retention after 10000 cycles. Also, insights into the charge storage mechanism and superb cycling stability of our new polymer cathode are given.

## 1. Introduction

The family of aqueous rechargeable batteries have intriguing advantages in terms of high safety, low cost, high power resulted from the fast electrochemical kinetics, and the potential for stationary energy storage [1–5]. Differing from alkali-ion-based batteries operating with single-electron transfer, multivalent ion aqueous batteries based on Zn<sup>2+</sup>, Mg<sup>2+</sup>, or Al<sup>3+</sup>, open opportunities for developing more advanced batteries by harnessing the multielectron transfer mechanism [6–8]. Among them, zinc metal has good compatibility with water, low redox potential (–0.76 V vs. standard hydrogen electrode), and high theoretical capacity (819 mAh g<sup>-1</sup> or 5845 mAh cm<sup>-3</sup>) [9], hence aqueous rechargeable Zn-ion batteries (ZIBs) have attracted much attention. However, a major drawback of aqueous batteries is the low energy density due to the limited voltage, as the water electrolysis threshold is ~1.23 V. Thus, the strategy for boosting the specific energy relies on either increasing the specific capacity of electrode or lifting up the operating voltage. For aqueous ZIBs of various types that were recently reported, an emerging

problem is that the Zn-based batteries suffer from the lack of high-performance cathode materials [10]. Also, the growth of Zn dendrites over the anode surface in some ZIBs is a problem to be solved [11, 12]. Therefore, exploring new cathode materials to make aqueous rechargeable ZIBs with both high capacity and long life is of great importance.

Some transition metal oxides, such as MnO<sub>2</sub> and V<sub>2</sub>O<sub>5</sub>, have been used to make ZIBs. Because the repeating insertion and extraction of ions in crystalline compounds can cause irreversible structural collapse, the inorganic cathode material generally suffers from significant capacity fading with cycling. Also, such metal oxides have high resistance, making them difficult to achieve a high mass loading (>10 mg cm<sup>-2</sup>) over the current collector substrate while maintaining a low internal resistance. Regarding the operating voltage, aqueous Zn//MnO<sub>2</sub> and Zn//V<sub>2</sub>O<sub>5</sub> cells were charged/discharged within voltage ranges of 1.0 – 1.8 V and 0.5 – 1.4 V, respectively [13,14]. Such narrow voltage windows are inadequate to render high power output, as the voltage gap between anode and cathode, ΔV, is related

\* Corresponding author.

E-mail address: [ljj78@buaa.edu.cn](mailto:ljj78@buaa.edu.cn) (J. Liu).

<https://doi.org/10.1016/j.ensm.2020.03.001>

Received 16 October 2019; Received in revised form 27 February 2020; Accepted 1 March 2020

Available online 3 March 2020

2405-8297/© 2020 Published by Elsevier B.V.

to the power capability. Very recently, Li et al. reported a  $\text{Zn}^{2+}/\text{Mn}^{2+}$  hybrid battery with using an aqueous electrolyte containing  $\text{ZnSO}_4$  and  $\text{MnSO}_4$  in the  $\text{Zn}/\text{MnO}_2$  cell, achieving a wide voltage window of 2.3 V and excellent cycling performance [15]. However, the capacitance retention was only 33% when current density was increased from 1 to 3  $\text{mA cm}^{-2}$ , suggesting a poor rate performance. Ding et al. reported a novel aqueous  $\text{Zn}/\text{VO}_2$  battery with ultrafast  $\text{Zn}^{2+}$  intercalation/deintercalation kinetics in  $\text{VO}_2$  [16], yet the 1.2 V voltage window is relatively narrow. Organic electrode materials are superior to the inorganic counterparts in terms of low cost, low toxicity, light weight, structural diversity, and molecular-level controllability [17]. Moreover, the long  $\pi$ -electron conjugated structure of conducting polymers, such as polyaniline (PANI), provides active groups that may have different redox potentials, leading to multiple voltage plateaus in the discharge profile [18,19]. So far, PANI, polypyrrole, and poly(3,3'-dihydroxybenzidine), have been used to be the cathode to match with the Zn anode for building aqueous ZIBs with operating voltage ranges of 0.5 – 1.5 V, 0 – 1.2 V, and 0.5 – 1.5 V, respectively [18,20,21]. Redox-active organic electrode materials can be classified as amino-containing aromatics and quinones, and their electrochemical behaviors vary greatly. Most organic electrode materials show unsatisfactory cycling life [22,23], and factors leading to the capacity fading remain unknown. Hence, obtaining a polymer electrode with superb cycling stability would help understand the mechanism of capacity decay in organic electrodes.

Herein, we report an aqueous Zn-organic cell with high specific capacity, high mass loading of the cathode material, good rate performance, and long cycling life. Poly(1,5-naphthalenediamine, NAPD) nanorods supported by nanoporous activated carbon (AC) granules were used as the high-capacity cathode material to make ZIBs operated within a relatively wide voltage range of 0.1 – 1.8 V. Two types of current collectors, the flexible carbon fiber fabric and the thick carbon felt, were used to make ZIBs in different forms. Without any treatment of the bare Zn foil, the cell showed super long cycling life over 10000 cycles. The mechanism of charge storage is discussed in detail.

## 2. Experimental

### 2.1. Materials

AC powder (YP-80, Kuraray Co.), carbon fabric (WOS1009, CeTech. Co.), and inexpensive carbon fiber felt were purchased from the market. The 1,5-NAPD monomer was purchased from Aladdin Co., China.

### 2.2. Electropolymerization of Poly(1,5-NAPD)

First, a slurry made by dispersing AC powder, carbon black, and poly(vinylidene fluoride) as binder at a weight ratio of 8:1:1 into N-methyl pyrrolidone. Second, the slurry was applied onto a rectangular carbon fiber fabric by using a pipette, followed by a drying process (Fig. S1). Third, the AC-coated carbon fabric was used as work electrode in a three-electrode cell containing 1 M  $\text{H}_2\text{SO}_4$  and 0.03 M 1,5-NAPD small molecules. With using a Pt foil as counter electrode and an Ag/AgCl reference electrode, the electropolymerization was conducted by running CV test at 20  $\text{mV s}^{-1}$  and within the voltage range from – 0.4 to 1.0 V for 300 cycles. Finally, the poly(1,5-NAPD)/AC substrate was removed out and rinsed with using deionized water, and then dried. The net weight of poly(1,5-NAPD)/AC was measured by using a 0.01 mg-resolution balance. Similarly, we also electrodeposited poly(1,5-NAPD) films onto Pt foils for Raman and X-ray photoelectron microscopy (XPS) measurements (Fig. S19a). To make a high-capacity cathode using carbon fiber felt as the current collector, the AC slurry was applied onto a piece of carbon fiber felt. This coating process can be repeated for several times to increase the mass loading of AC. Then, the dried AC@carbon felt substrate was immersed into a three-electrode cell for conduct the electrodeposition of poly(1,5-NAPD).

### 2.3. Fabrication of ZIBs

To make a flat pouch cell, a poly(1,5-NAPD)/AC cathode, a glass fiber membrane soaked with 2 M  $\text{ZnSO}_4$  solution, and an 80- $\mu\text{m}$ -thick Zn foil were stacked together and then sealed between two Al-plastic films with using hot melting glue. Note that the Zn foil can provide an areal capacity of 29  $\text{mAh cm}^{-2}$  in theory, which is much surplus to the cathode capacity in our experiment. The two electrodes and a separator were also punched to collect disk-shaped pieces, which were assembled into a CR2025-type button cell. To make a cable-shaped ZIB, a Zn wire was wrapped by a glass fiber membrane. After applying a gelled electrolyte made by dissolving polyvinyl alcohol in the  $\text{ZnSO}_4$  solution, the membrane was covered by a carbon-fabric-supported poly(1,5-NAPD)/AC cathode. The device was encapsulated into a heat shrinkable plastic tube.

## 3. Results and discussion

### 3.1. Structural characterization

The fabrication process of a  $\text{Zn}/\text{poly}(1,5\text{-NAPD})/\text{AC}$  cell is illustrated in Fig. 1a. A carbon-fabric-supported poly(1,5-NAPD)/AC cathode, of which an optical photograph is shown in Figs. S2c and a Zn foil anode are assembled together with an in-between glass fiber membrane soaked with  $\text{ZnSO}_4$  aqueous electrolyte. Fig. 1b shows a scanning electron microscopy (SEM) image of the bare AC coating on carbon fabric. Low-magnification images of AC coatings with different mass loadings on carbon cloth can be found in Figs. S2d and f. These AC granules are several micrometers in size. The morphology of electrodeposited poly(1,5-NAPD) over AC granules is depicted in Fig. 1c and d. The commercial AC powder has a high specific surface area of  $\sim 2280 \text{ m}^2 \text{ g}^{-1}$  and a BJH desorption average pore size of 2.1 nm (Figs. S5a and b). The AC coating has a reduced specific surface area of  $1820 \text{ m}^2 \text{ g}^{-1}$ , but its average pore size was slightly increased to 2.4 nm (Figs. S5a and c). After the deposition of poly(1,5-NAPD), the specific surface area of the composite coating was largely reduced to be  $141 \text{ m}^2 \text{ g}^{-1}$ , and the average pore size was increased to 6.0 nm (Figs. S5a and d). Hence, the polymer is believed to be not only filled into the nanopores, but also coated onto the outer surfaces of AC granules. Note that small 1,5-NAPD molecules dissolved in water can be naturally adsorbed onto AC granules. The AC coating with adsorbed 1,5-NAPD molecules shows a specific surface area of  $1151 \text{ m}^2 \text{ g}^{-1}$  and an average pore size of 4.7 nm (Figs. S5e and f). It indicates that, by filling organic molecules into the nanopores of AC granules, the average pore size can be increased. Our explanation is that, micropores with size equivalent to the organic molecule size could be blocked and are excluded in the calculations of both surface area and average pore size of AC granules, as illustrated in the inset in Fig. S5f, thus the AC coatings with electrodeposited poly(1,5-NAPD) or adsorbed 1,5-NAPD molecules have reduced surface area and increased average pore size. Similar to the electropolymerized poly(1,5-NAPD), the 1,5-NAPD small molecules adsorbed onto AC granules also have an effect on enhancing the charge storage capacity (Fig. S8). The high-magnification SEM image in Fig. 1d shows that the poly(1,5-NAPD) nanorods are about 100 – 150 nm in thickness and several hundreds of nm in length. It should be addressed that this polymer was electrodeposited by continuously running the cyclic voltammetry (CV) test. During the electrodeposition process, the morphology evolution of poly(1,5-NAPD) over AC granules with prolonging the electropolymerization time is shown in Fig. S3. At early stage, poly(1,5-NAPD) nanodots over the AC surface were emerged. Because this polymer tends to grow into 1D structure, the continuous growth of nanodots leads to the formation of nanorod arrays standing over the AC surface. Two close-view SEM images in Figs. S4a and b show the electrodeposited poly(1,5-NAPD) nanorods at early and mature stages, respectively. A transmission electron microscopy image of these nanorods is shown in Fig. S4c. Note that the AC granule not only favors the growth of poly(1,5-NAPD) nanorod arrays, but also helps increase the mass gain of poly(1,5-

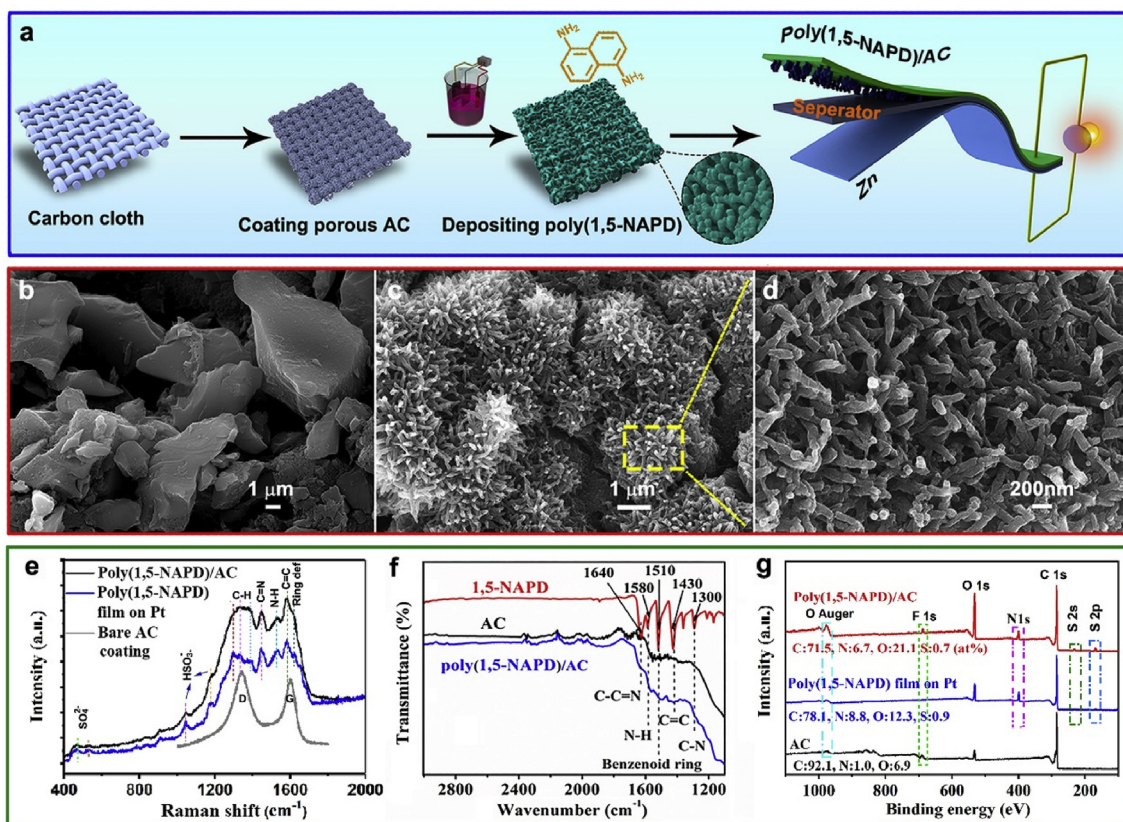


**Fig. 1.** (a) Illustration for the fabrication process of a sandwich-structured Zn-ion cell using poly(1,5-NAPD)/AC composite as the cathode material. (b) SEM image of the nanoporous AC coating on carbon fabric. (c and d) Low- and high-magnification SEM images of the electrodeposited poly(1,5-NAPD) over AC granules, respectively. (e) Raman spectra of poly(1,5-NAPD)/AC cathode, poly(1,5-NAPD) film on Pt, and AC coating. (f) FTIR spectra collected from 1,5-NAPD monomer, pure AC, and poly(1,5-NAPD)/AC composite. (g) XPS spectra of poly(1,5-NAPD)/AC cathode, poly(1,5-NAPD) film on Pt, and AC coating.

NAPD), which is important for enhancing the capacity. For comparison, we also directly electrodeposited poly(1,5-NAPD) onto a bare carbon cloth (CC). SEM images of this sample, named as poly(1,5-NAPD)/CC, are shown in Figs. S24a, b, and c. As a result, the mass loading of poly(1,5-NAPD) is around  $1 \text{ mg cm}^{-2}$  and no nanorod arrays formed over the carbon fiber (Fig. S24c). Such a low mass loading of electrode material is inadequate for practical application.

Fig. 1e shows three Raman spectra (laser wavelength 633 nm) collected from a poly(1,5-NAPD)/AC cathode, an electrodeposited poly(1,5-NAPD) film on Pt foil, and a bare AC coating, respectively. The AC base shows characteristic D and G bands of graphitic carbon. However, the Raman spectra of poly(1,5-NAPD)/AC and pure poly(1,5-NAPD) film on Pt show more peaks. The pronounced peak at  $1586 \text{ cm}^{-1}$  is assigned to the stretching vibration of C=C bonds [24], and the broad band at  $1300\text{--}1400 \text{ cm}^{-1}$  is related to the C-H bending mode [25]. The two peaks at  $1450$  and  $1530 \text{ cm}^{-1}$  are assigned to C=N stretching vibration and N-H bending vibration, respectively [26]. Four weak peaks at  $460$ ,  $530$ ,  $1045$ , and  $1180 \text{ cm}^{-1}$ , respectively, are contributed by surface-adsorbed sulfate ions [27]. Fig. 1f shows the Fourier transform infrared (FTIR) spectra of poly(1,5-NAPD)/AC cathode, bare AC, and 1,5-NAPD monomer, respectively. The poly(1,5-NAPD) shows weak peaks related to C=N, N-H, and C-N bonds in the FTIR spectrum due to the strong light absorption of the black AC base. In addition, the surface chemistry of a poly(1,5-NAPD)/AC cathode was studied by using XPS, as shown in Fig. 1g. For comparison, two XPS spectra from a pure poly(1,5-NAPD) film on Pt and a bare AC coating, respectively, are shown as well. The N contents in poly(1,5-NAPD)/AC, poly(1,5-NAPD)/Pt, and bare AC samples are 6.7, 8.8, and 1.0 atom %, respectively, given by the XPS analysis. The strong N signal is contributed by the amino-containing poly(1,5-NAPD). The weak S and F signals can be attributed to residual

$\text{SO}_4^{2-}$  in the cathode surface and poly(vinylidene fluoride) as binder in the AC base, respectively. The electrodeposited poly(1,5-NAPD) is amorphous, as only two broad peaks from the graphitic carbon cloth base are emerged in the X-ray diffraction (XRD) pattern (Fig. S6).

### 3.2. Zn//Poly(1,5-NAPD)/AC cells using carbon cloth as the current collector

Aqueous Zn//poly(1,5-NAPD)/AC cells were assembled and encapsulated into flat pouches for studying their electrochemical performances. First, the optimal electrolyte was determined by comparing the efficacies of three aqueous electrolytes,  $\text{ZnSO}_4$ ,  $\text{ZnCl}_2$ , and  $\text{Zn}(\text{CF}_3\text{SO}_3)_2$  (zinc trifluoromethanesulfonate). CV and galvanostatic charge/discharge (GCD) curves of three cells using different electrolytes are shown in Figs. S7a and b, respectively. The suitable voltage range of the cell using  $\text{ZnCl}_2$  electrolyte is  $0.1\text{--}1.3 \text{ V}$ . Beyond this range, the evolution of  $\text{Cl}_2$  and  $\text{H}_2$  in electrolyte would occur. By using  $\text{ZnSO}_4$  or  $\text{Zn}(\text{CF}_3\text{SO}_3)_2$  electrolytes, the operating voltage can be extended to  $1.8 \text{ V}$ . However, compared to  $\text{Zn}(\text{CF}_3\text{SO}_3)_2$ , the use of  $\text{ZnSO}_4$  electrolyte leads to a higher discharge voltage plateau and a larger charge storage capacity, as shown in Fig. S7b. Therefore, the  $\text{ZnSO}_4$  electrolyte was used in all devices in the following experiments. More CV loops of our ZIBs with using different electrolytes can be found in Figs. S7c, d, e, and f. Introducing poly(1,5-NAPD) to the nanoporous AC can largely increase the capacity, as the area of CV loop is much larger than that of a Zn//AC hybrid supercapacitor when at identical voltage scan rate (Fig. S8a).

The mass gain of electrodeposited poly(1,5-NAPD) is a function of the AC mass loading. For instance, the polymer takes 53 wt% in a poly(1,5-NAPD)/AC cathode coating with mass loading of  $2.7 \text{ mg cm}^{-2}$ . But the polymer content is reduced to 41 wt% with increasing the mass loading

of poly(1,5-NAPD)/AC composite to  $11.8 \text{ mg cm}^{-2}$ . For the ZIB with low mass loading of poly(1,5-NAPD)/AC in the cathode ( $2.7 \text{ mg cm}^{-2}$ ), its rate performance is shown in Fig. 2a, revealing a maximum specific capacity of  $315 \text{ mAh g}^{-1}$  at  $0.19 \text{ A g}^{-1}$ . Here the gross weight including AC coating and poly(1,5-NAPD) was used to calculate the gravimetric specific capacity. Furthermore, the nearly 100% Coulombic efficiency indicates that the wide voltage window of  $1.7 \text{ V}$  is appropriate and the water electrolysis is ruled out. Fig. 2e shows GCD profiles of this cell at different current densities. Besides the high specific capacity, our poly(1,5-NAPD)/AC cathode also shows good rate capability. For instance, with increasing the current from  $0.19$  to  $14.8 \text{ A g}^{-1}$  (by 78 times), its specific capacity is dropped from  $315$  to  $145 \text{ mAh g}^{-1}$  (46% retention). Such a rate performance is superior to those of most ZIBs ever reported [3,15,18,19]. In Fig. 2a, when the current was back to  $0.19 \text{ A g}^{-1}$ , the capacity was recovered to  $307 \text{ mAh g}^{-1}$  (97% of the original value), showing excellent endurance to high-speed reaction. Apart from the high specific capacity, our ZIB also shows long-term cycling stability, as shown in Fig. 2h. After running the GCD test at  $10 \text{ A g}^{-1}$  for 10000 cycles, the capacity retention was ended at 91% and the Coulombic efficiency remained to be 100%. For other Zn-based batteries including Zn-MnO<sub>2</sub> and Zn-Ni systems, the growth of Zn dendrites is a major issue that may disable the cell after a few hundreds of cycles [22,23,28]. In our work, after the long-term cycling process, Zn dendrites were not observed from the surface of Zn anode (Fig. S9). Also, the morphology of poly(1,5-NAPD) nanorods remained unchanged, evidenced by their SEM images before and after

the cycling test (Fig. 2h and Fig. S23).

To further investigate the electrochemical behavior, a group of CV curves at scan rates from  $0.2$  to  $1.0 \text{ mV s}^{-1}$ , as shown in Fig. 2b, are used to study the relationship between redox peak current  $i$  and potential sweep rate  $\nu$ , which obeys the power-law relationship as  $i = a\nu^b$  [29,30], where  $a$  and  $b$  are adjustable parameters, and  $\nu$  is the voltage scan rate. When the  $b$ -value is 1, the current is surface-controlled, indicating supercapacitor-like electrochemical behaviors. When the  $b$ -value is 0.5, the current is controlled by semi-infinite linear diffusion, indicating a battery-like behavior. The CV loop shows an oxidation peak (O) and a reduction peak (R). By correlating  $\log(i)$  and  $\log(\nu)$ , the  $b$ -values are obtained to be 0.84 for the O peak and 0.83 for the R peak by linear fitting, as shown in Fig. 2c. Therefore, for this device with cathode mass loading of  $2.7 \text{ mg cm}^{-2}$ , the interface pseudocapacitance plays a dominant role in energy storage. The specific percentage of the surface-controlled capacity can be calculated by using the equation  $i = k_1\nu + k_2\nu^{0.5}$ , where  $k_1\nu$  and  $k_2\nu^{0.5}$  represent the surface-controlled capacity and the semi-infinite linear diffusion contribution, respectively [31]. Hence, the contribution percentage of surface-controlled capacity can be obtained (Fig. S10). As shown in Fig. 2d, with increasing the voltage scan rate from  $0.2$  to  $1.0 \text{ mV s}^{-1}$ , the percentage of pseudocapacitive contribution was increased from 64.8 to 78.2%. The high proportion of surface-controlled pseudocapacitance for this poly(1,5-NAPD)/AC cathode results in fast ion kinetics, benefiting the power capability. However, the  $b$ -value is a function of the areal mass loading of

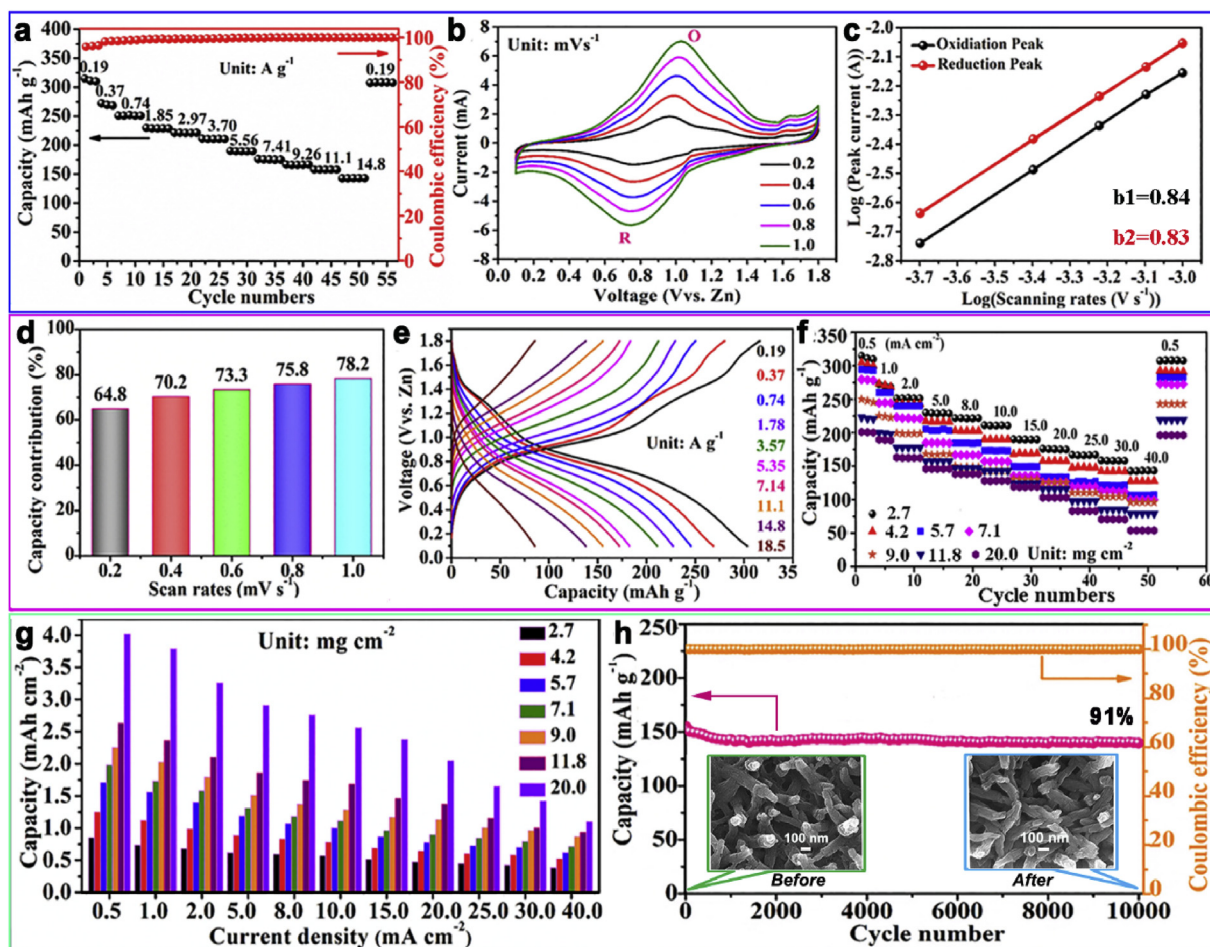


Fig. 2. (a) Rate performance of a typical ZIB with poly(1,5-NAPD)/AC mass loading of  $2.7 \text{ mg cm}^{-2}$ . (b) CV curves of this cell, according to which the  $b$ -values for O and R peaks are deduced, as shown in (c). (d) Surface-controlled capacity contributions at different scan rates. (e) Charge/discharge profiles of the cell at different current densities. (f) Rate performances of a groups of Zn//poly(1,5-NAPD)/AC cells with different mass loadings of the cathode material. (g) Areal capacities of these cells at different current densities. (h) Cycling stability of a typical button-type cell tested at  $10 \text{ A g}^{-1}$  over 10000 cycles. The insets depict the poly(1,5-NAPD) nanorods before and after the long-term cycling test.

cathode material. A trend is that the thicker the cathode coating, the lower the b-value. For e.g., when the cathode mass loading was increased to  $\sim 7 \text{ mg cm}^{-2}$ , the b-value for the O peak was decreased to 0.7 (Fig. S11), suggesting a trend towards battery-like behavior.

A high mass loading of electrode material is important for rendering high energy storage capacity of a battery. We made a group of aqueous ZIBs with different mass loadings of the cathode material, ranging from 2.7 to 20  $\text{mg cm}^{-2}$ , and compared their energy storage performances. As shown in Fig. 2f, our Zn//poly(1,5-NAPD)/AC cells maintained good rate performance regardless of the thickened cathode coating. For the thickest cathode with poly(1,5-NAPD)/AC mass loading of 20  $\text{mg cm}^{-2}$ , the specific capacity was 4.0  $\text{mAh cm}^{-2}$  at 0.5  $\text{mA cm}^{-2}$ . More importantly, the areal capacity of this cell still maintained high even at high current, as 1.1  $\text{mAh cm}^{-2}$  when at 40.0  $\text{mA cm}^{-2}$ .

Fig. 3 shows Ragone plots of these Zn//poly(1,5-NAPD)/AC cells with different mass loadings of the cathode material. In Fig. 3a, the maximum gravimetric energy densities of this group of ZIBs are confined within a narrow range from 150 to 200  $\text{Wh kg}^{-1}$ , while the maximum power densities are distributed within a wide range from 10 to  $10^4 \text{ W kg}^{-1}$ . For comparison, energy and power densities of some other devices, including Li-ion battery, redox flow battery, lead-acid battery, NiMH battery, and commercial supercapacitors and ordinary capacitors, are marked as well in Fig. 3a [32]. It can be concluded that our ZIBs are comparable to Li-ion batteries in terms of gravimetric energy density and have supercapacitor-level power capability. The specific energy of our device also surpasses those of most other Zn–organic or Zn–inorganic batteries ever reported. For e.g., Ghanbari et al. assembled ZIBs with using the PANI/graphite composite as a cathode, and their device exhibited an energy density of 162  $\text{Wh kg}^{-1}$  [33]; Guo et al. reported rechargeable Zn//pyrene-4,5,9,10-tetraone batteries with a maximum specific energy of 186  $\text{Wh kg}^{-1}$  or 1.55  $\text{mWh cm}^{-1}$  [34]. The specific energy of our device is also comparable to those of other aqueous ZIBs using metal-oxide-based cathodes. More comparisons can be found in Table S1. The areal energy density can be increased by adding the mass loading of cathode material, as shown in Fig. 3b. The cell with the highest mass loading of cathode material exhibited a maximum areal energy density of 3.2  $\text{mWh cm}^{-2}$ . All cells show high areal power densities up to 60  $\text{mW cm}^{-2}$ .

### 3.3. Electrochemical performances of Mechanically bent Zn//Poly(1,5-NAPD)/AC cells

We made two types of flexible quasi-solid ZIBs using the poly(1,5-NAPD)/AC cathode, the flat pouch cell and the cable-shaped cell. Both were continuously charged/discharged while bent at different angles, as shown in Fig. 4. During the cycling process, the Coulombic efficiency and specific capacitance of the pouch cell remained stable regardless of bending (Fig. 4a). The nearly 100% Coulombic efficiency rules out the

water decomposition inside the cell when charged to 1.8 V. For the cable-shaped cell with a Zn wire in the center, it showed capacity decay during the first 200 cycles. In the following cycles, its capacity and Coulombic efficiency remained stable even bent at large angles up to  $180^\circ$ , as shown in Fig. 4d. Hence, the capacity decay of this cell at early stage of cycling is unlikely caused by bending. To demonstrate the practical application, two pouch cells were connected in series to power up a string of violet LEDs (Fig. 4b). Also, two curved cable-type cells in series were used to light up a red LED, as shown in Fig. 4e. The structure of our cable-shaped ZIB is illustrated in the inset. For endurance test, a pouch cell and a cable-type cell were repeatedly bent at  $180^\circ$  and then straightened for 150 cycles. GCV curves at 5  $\text{mA cm}^{-2}$  were collected from the two devices after different bending cycles, and the results are shown in Fig. 4c and f, respectively. It can be seen that the capacity was slightly reduced by repeatedly bending the device. Both cells showed an identical capacity retention of 92% after 150 bending cycles. It is worth mentioning that the Zn foil or wire could be broken with adding the bending cycles due to the metal fatigue.

### 3.4. Zn//Poly(1,5-NAPD)/AC cells using carbon fiber felt as the current collector: Potential for large-scale energy storage

Grid energy storage requires safe and durable batteries, of which the volumetric energy density is a minor issue. The carbon felt with millimeter-scale thickness consists of entangled graphitic micro fibers and is highly conductive, inexpensive, and compressible. The price of carbon felt is about 1/20 of that of the conductive carbon cloth. Here, we demonstrate the use of carbon fiber felt as current collector to support poly(1,5-NAPD)/AC with high mass loading. The photograph in Fig. 5a shows two 3 mm-thick carbon felts with and without the composite cathode material, respectively. Typical SEM images of the carbon felt loaded with AC are shown in Figs. S2h and i. In a beaker-based two electrode cell, a carbon-felt-based cathode was surrounded by a U-shaped Zn foil, forming a high-capacity prototype cell. As a demonstration of practical application, two such cells were connected in series to double the output voltage, as illustrated in Fig. 5e. As a result, a string of red LEDs was lit up over 4 h (Fig. 5b and Supporting Video), indicating high energy storage capacity. Moreover, all stored energy in our ZIB can be released in a few minutes, indicating high power capability. For instance, the two cells in Fig. 5b were also used to drive a mini electric fan for 5 min until exhausted (Fig. S12 & Supporting Video). Fig. 5c shows GCD curves of the carbon-felt-based cathode, which are a bit straighter than those of the carbon-fabric-based cathode in Fig. 2e. This cathode exhibits a high areal capacity of 9.2  $\text{mAh cm}^{-2}$ , corresponding to an energy density of 7.7  $\text{mWh cm}^{-2}$  (Fig. S13). Fig. 5g and h show CV and GCD curves of two identical cells in series, respectively, with an operating voltage range of 0.2–3.6 V. Note that the CV curve at a low voltage scan rate of 2  $\text{mV s}^{-1}$  shows no polarization tendency when approaching 3.6 V.

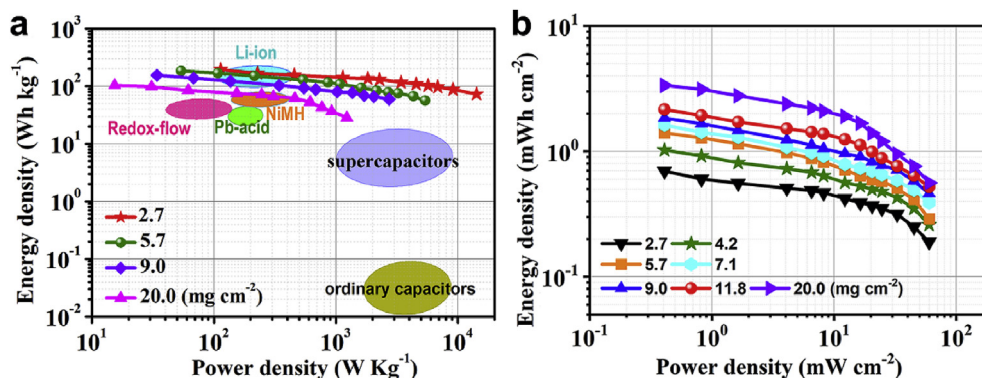


Fig. 3. Ragone plots showing the energy and power densities of a group of Zn//poly(1,5-NAPD)/AC cells with different mass loadings of the cathode material on carbon fabric. (a) Gravimetric densities. Values of some other devices are marked as well for comparison. (b) Areal densities.

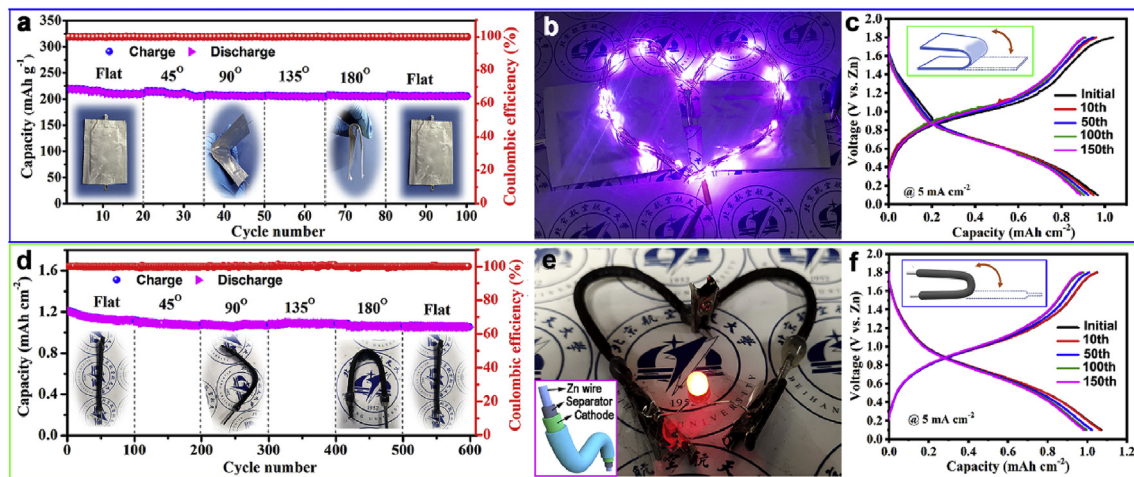


Fig. 4. (a) Cycling stability of a flat pouch ZIB that was bent at different angles. (b) Violet LEDs powered up by using two pouch cells in series. (c) GCD curves collected after repeatedly bending a pouch cell for different cycles, as illustrated in the inset. (d) Cycling stability of a bendable cable-shaped Zn-ion cell that was bent at different angles. (e) A red LED lit up by two cable-type Zn-ion micro cells in series. (f) GCD curves of a cable-type ZIB after being repeatedly bent over different cycles. (For interpretation of the references to color in this figure legend, the reader is referred to the Web version of this article.)

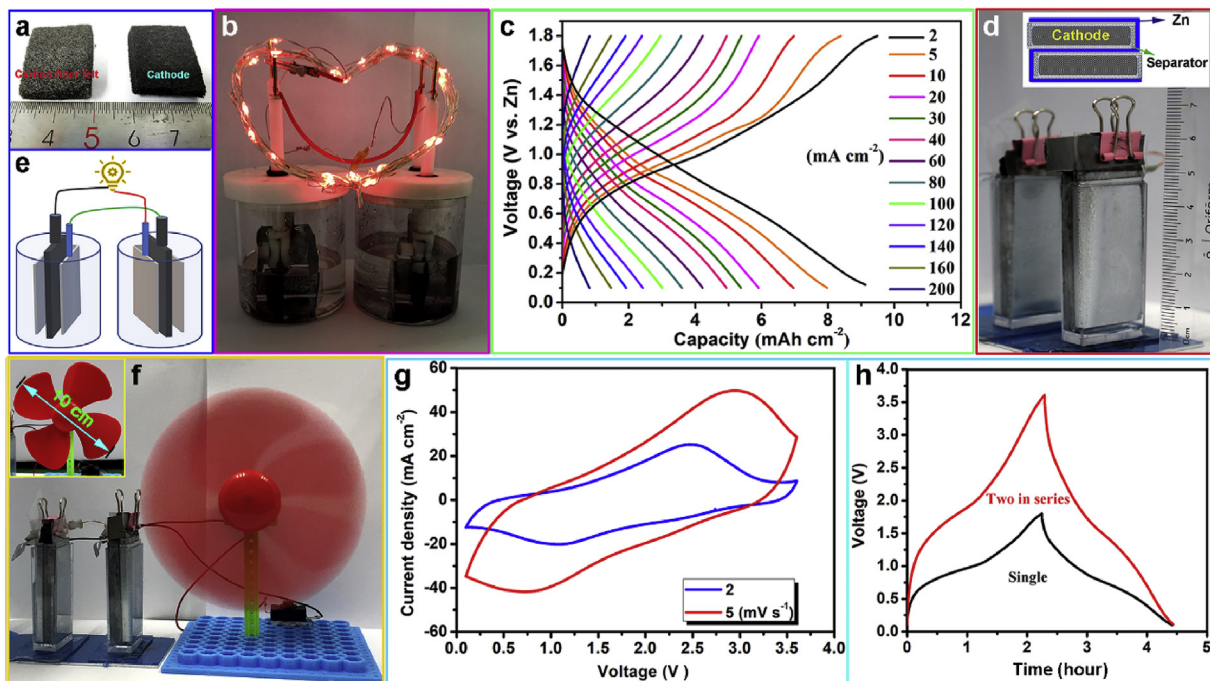


Fig. 5. (a) optical photograph showing two 3 mm-thick carbon fiber felt with and without loading the poly(1,5-NAPD)/AC cathode material, respectively. (b) Two beaker-based ZIBs used to light up a string of LEDs for over 4 h. Illustration for this tandem connection is shown in (e). (c) GCD profiles of a single cell using carbon felt as current collector. (d) Photograph of two mini cells containing compactly stacked electrodes. The arrangement of Zn foil and carbon-felt-based cathode is illustrated in the inset. (f) An electric fan powered up by using the two mini cells in series. (g and h) CV and GCD curves of two identical Zn-ion cells in series, respectively.

The CV loop at  $5 \text{ mV s}^{-1}$ , which is too fast to be implemented on conventional Li-ion batteries, suggests a pseudocapacitive behavior [35]. The high power density of our ZIB based on carbon felt is attributed to its dominant pseudocapacitive behavior, which is reflected by the high b-value of 0.85 (Fig. S12f), though the mass loading of poly(1,5-NAPD)/AC in the felt is as high as  $35 \text{ mg cm}^{-2}$ . It can be understood that the poly(1,5-NAPD)-modified AC granules inside the carbon felt are well soaked with electrolyte, facilitating the interfacial Faradaic process. The carbon-felt-based cathode integrated into a button-type ZIB also exhibits excellent cycling stability. After being cycled at  $50 \text{ mA cm}^{-2}$  for 10000 cycles, the capacity retention was  $\sim 100\%$  (Fig. S12g).

Supplementary video related to this article can be found at <https://doi.org/10.1016/j.ensm.2020.03.001>

[i.org/10.1016/j.ensm.2020.03.001](https://doi.org/10.1016/j.ensm.2020.03.001)

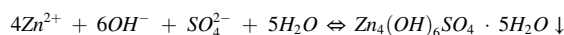
Multiple cathodes and anodes can be compactly stacked to reduce to the cell volume, as demonstrated in Fig. 5d. The inset illustrates the compact arrangement of electrodes. In the mini cell enclosed by using a small plastic cuboid box, each cathode has an effective area of  $2.2 \times 4.5 \text{ cm}^2$ . Using the volume of small cuboid box, the volumetric energy density of a mini cell is estimated to be  $25 \text{ Wh L}^{-1}$  (Fig. S14b). Note that the carbon felt is compressible. If such electrodes are squeezed in a battery pack, the volumetric energy density could be easily doubled. As a demonstration of practical application, an electric mini fan with diameter of 10 cm was powered up for 25 min by the two Zn-ion mini cells in series (Fig. 5f).

Although the median voltage of our ZIB is below 1 V, lower than those of Zn//MnO<sub>2</sub> and Zn//prussian blue batteries [36], its energy storage capacity deduced from the area below a GCD curve is relatively high, owing to the high specific capacity of the poly(1,5-NAPD)/AC cathode. In general, multiple cell units are connected to multiply the voltage output of a commercial battery pack, hence the low operating voltage of a single cell would be not a major issue, compared to other aspects such as cost, energy density, and cycling life. The use of prussian-blue-based cathode to match with Zn can lead to a high discharge voltage plateau from 1.75 to 1.66 V, yet the specific capacity at 1 C was 65 mAh g<sup>-1</sup> and the capacity retention was 76% after 100 cycles [37]. Differing from other ZIBs based on inorganic compound cathodes, our device in fact has a hybrid energy storage mechanism, as the slope-shaped discharge profile is analogous to that of a supercapacitor. For a pack of such ZIBs in series connection, an electronic circuit board named constant voltage converter can be added to ensure a stable voltage output.

### 3.5. Insights into the charge storage mechanism

To have an insight into the energy storage mechanism of our Zn//poly(1,5-NAPD)/AC cell, we used ex situ XPS and XRD to study the cathode at different states in a CD cycle, as marked in Fig. 6a. The cathode in a beaker-based two-electrode cell was discharged from 1.8 V to 0.1 V, and then charged to 1.8 V. During this process, the cell was disconnected at a certain voltage point, and the cathode was removed out to have a small piece cut off by using ceramic scissors. The small piece of cathode was rinsed by using deionized water and then dried for characterizations. In Fig. 6b, the ex situ XPS spectra corresponding to

different states show Zn 2p, O 1s, N 1s, and C 1s peaks. However, when discharged from 1.8 V to 0.1 V, the Zn, O, and S signals were gradually enhanced while the intensity of C signal remained rather stable. In the following charging process from 0.1 V to 1.8 V, the Zn, O, and S signals were weakened. The ex situ XRD measurements revealed that some sharp peaks were emerged when the cathode was at discharged state, as shown in Fig. 6c. The broad XRD peak around 26° is contributed by the carbon fiber fabric base. The sharp peaks are contributed by an inorganic byproduct formed via the reaction [38,39]:



Interestingly, the formation of these inorganic flakes is reversible at early stage of cycling, as their alternate emergence and disappearance are evidenced by both SEM observation and ex situ XRD measurements. In the XRD patterns in Fig. S15 that were collected in the first two cycles, these sharp peaks were emerged when the cathode was fully discharged (0.1 V), while disappeared when at fully charged state (1.8 V). However, the dissolution and formation of these byproduct flakes are partially reversible. In the following long-term cycling process, they continued to grow and finally reached a saturation size. A similar phenomenon was also found from Zn//AC and MnO<sub>2</sub>//AC hybrid supercapacitor with using ZnSO<sub>4</sub> electrolyte [38,40], and the dissolution of Zn<sub>4</sub>(OH)<sub>6</sub>SO<sub>4</sub>•5H<sub>2</sub>O was attributed to the reduced pH value of the electrolyte when the cell is charged. For a Zn//AC hybrid supercapacitor, both H<sup>+</sup> and Zn<sup>2+</sup> can be physically adsorbed onto the nanoporous cathode when discharged, and the released H<sup>+</sup> would etch those inorganic flakes during the charging process. In our work, the poly(1,5-NAPD)/cathode has a low specific surface area of 141 m<sup>2</sup> g<sup>-1</sup>, and the released H<sup>+</sup> from the polymer

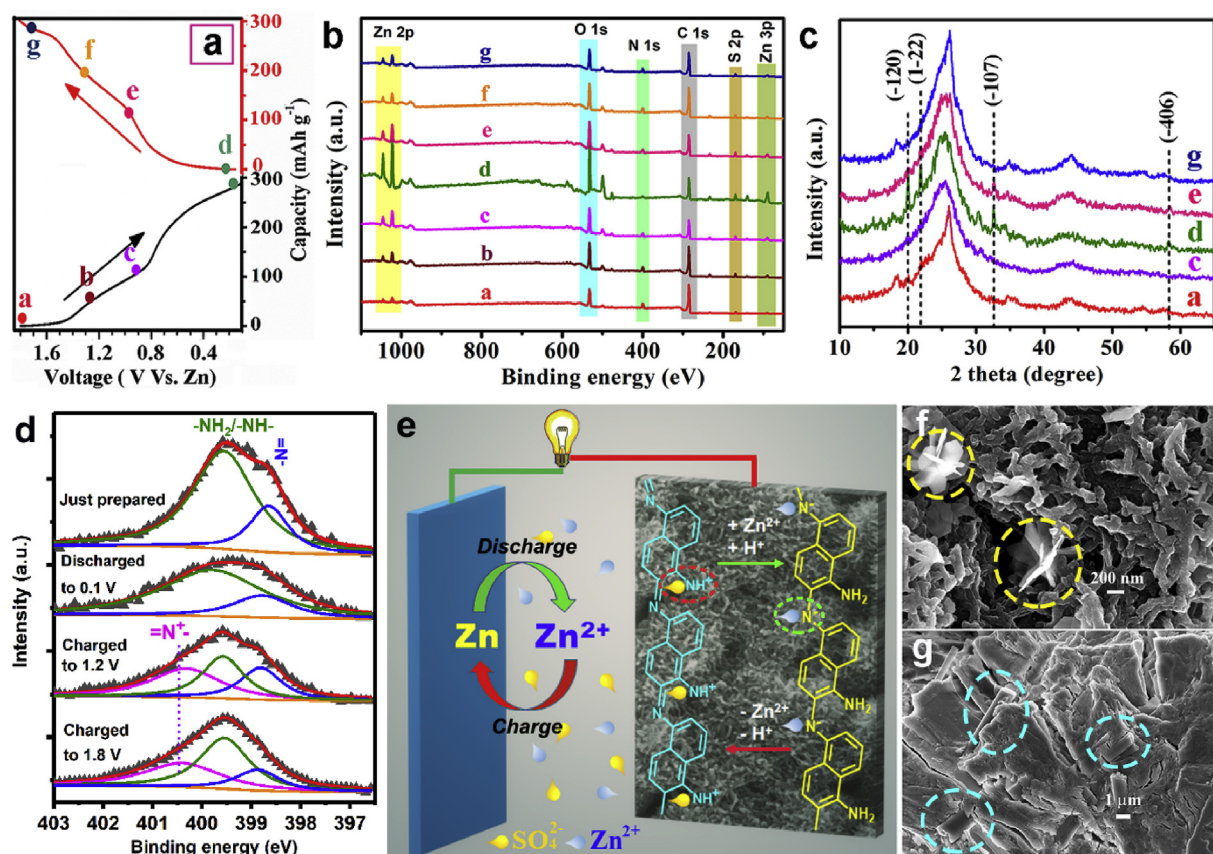


**Fig. 6.** (a) GCD curve at 0.2 A g<sup>-1</sup> from a Zn//poly(1,5-NAPD)/AC cell. Ex situ XPS and XRD spectra of the cathode at different states marked by color dots along the CD curve are shown in (b) and (c), respectively. (d) High-resolution N 1s XPS spectra from the cathode at different charge/discharge states. (e) Illustration for the charge storage mechanism. (f and g) SEM images of cathode and anode in a button cell after 10000 cycles, respectively. Some inorganic flakes in (f) are emphasized by using dashed-line circles. The circles in (g) indicate that some glass fiber fragments from the separator are embedded into the Zn foil after the cycling process. (For interpretation of the references to color in this figure legend, the reader is referred to the Web version of this article.)

would be responsible for the dissolution of  $\text{Zn}_4(\text{OH})_6\text{SO}_4 \bullet 5\text{H}_2\text{O}$  flakes.

To support our argument that both  $\text{Zn}^{2+}$  and  $\text{H}^+$  participate in the charge storage process, we tested a poly(1,5-NAPD)/AC cathode in a three-electrode cell filled with 1 M  $\text{H}_2\text{SO}_4$ , with using a Pt foil as counter electrode and an Ag/AgCl reference electrode. As shown in Fig. S16a, the voltage window can be extended from  $-0.2 - 0.8$  V for the bare AC electrode to  $-0.6 - 1.0$  V for the poly(1,5-NAPD)/AC electrode, and the redox peaks over the CV loop suggest a pseudocapacitive behavior of the polymer. The insertion of  $\text{H}^+$  into the polymer is responsible for the broadened voltage window, as it inhibits the evolution of  $\text{H}_2$  when the voltage is below  $-0.2$  V (Vs. Ag/AgCl) in  $\text{H}_2\text{SO}_4$  electrolyte. Moreover, the poly(1,5-NAPD)/AC electrode in  $\text{H}_2\text{SO}_4$  electrolyte shows good cycling performance, as the capacity retention was 103% after 10000 cycles (Fig. S16c). Therefore, when in the naturally acidic  $\text{ZnSO}_4$  electrolyte (pH  $\sim 5.4$ ), both  $\text{Zn}^{2+}$  and  $\text{H}^+$  can be inserted into the polymer and have contribution to the redox reaction. Using a beaker-based two-electrode cell filled with  $\text{ZnSO}_4$  electrolyte, a poly(1,5-NAPD)/Pt cathode and a poly(1,5-NAPD)/AC cathode at different charge/discharge states were studied by using ex situ Raman measurements, and the results are shown in Fig. S19. However, the changes of Raman signals during the charge/discharge process were difficult to discern. Because the redox process occurred at the outer surface of poly(1,5-NAPD) coating, Raman signals from charged/discharged molecules in the top layer with thickness of a few nm are mingled with the strong background signals contributed by deeper molecules as the majority within the depth of laser beam irradiation.

Now Fig. 6d and e are used to elucidate the charge/discharge process. The molecular structure of poly(1,5-NAPD) is proposed according to the theoretical simulation with minimum energy principle [41]. Fig. 6e shows ex situ N 1s XPS spectra collected from a poly(1,5-NAPD)/AC cathode at different charge/discharge states. For a freshly prepared sample, the signal from  $-\text{NH}_2$  or  $-\text{NH}-$  is dominant in the N 1s peak, and the other subpeak at 398.4 eV is contributed by  $\text{C}=\text{N}-$  bonds. Using the areas of two subpeaks, the ratio of  $\text{C}=\text{N}-$  to  $-\text{NH}_2/-\text{NH}-$  components is obtained to be 0.3:1. Note that the open circuit voltage of a freshly assembled Zn//poly(1,5-NAPD)/AC cell is  $\sim 1.2$  V. After the first discharge cycle from 1.2 to 0.1 V, the N 1s peak shows a reduced component ratio of  $\text{C}=\text{N}-$  to  $-\text{NH}_2/-\text{NH}-$ , as 0.15:1 when at 0.1 V. The combination of  $\text{C}=\text{N}-$  with intercalated  $\text{H}^+$  could be responsible for the reduced content of  $\text{C}=\text{N}-$  as well as the increased content of  $-\text{NH}-$ . The two subpeaks in the N 1s XPS spectrum of the cathode at 0.1 V are relatively broad and slightly shifted to higher energy positions, presumably because partial amino groups are negatively charged due to  $\text{Zn}^{2+}$  binding, as  $\text{C}=\text{N}- \rightarrow \text{C}=\text{N}^-$  and marked by the green dashed-line ellipse in Fig. 6e. When charged to 1.2 or 1.8 V, intercalated  $\text{Zn}^{2+}$  ions are released from the polymer. Also, dangling  $-\text{NH}_2$  groups would be oxidized by intercalated  $\text{SO}_4^{2-}$  to be  $-\text{NH}^+$  and release  $\text{H}^+$  ions into the electrolyte, as marked by the red dashed-line ellipse in Fig. 6e. The role of  $\text{SO}_4^{2-}$  in the energy storage process is confirmed by comparing two CV loops from two Zn//poly(1,5-NAPD)/AC cells with using  $\text{ZnCl}_2$  and  $\text{ZnSO}_4$  electrolytes, respectively (Fig. S7b). Therefore, for a charged cathode the component of  $-\text{NH}_2/-\text{NH}-$  is reduced in the N 1s peak, because the XPS signals from positively charged  $\text{C}=\text{N}^+$  or  $-\text{NH}^+$  are generally shifted to higher energy positions, compared to their neutral state [42]. In the following discharging process,  $\text{SO}_4^{2-}$  would be extracted from the polymer and the  $-\text{NH}^+$  groups gain electrons and combine with the intercalated  $\text{H}^+$  to form  $-\text{NH}_2$  groups again. Simultaneously, the intercalated  $\text{Zn}^{2+}$  ions are anchored at  $-\text{N}^-$  sites.

Fig. 6f and g depict the surfaces of a carbon-cloth-supported poly(1,5-NAPD)/AC cathode and a Zn foil anode in a button cell after 10000 cycles, respectively. Inorganic flakes with sizes around  $1 \mu\text{m}$  are parsley distributed over the cathode surface, as marked by the dashed-line circles. Using the energy dispersive X-ray spectroscopy (EDS), elemental mappings of the charged poly(1,5-NAPD)/AC cathode after long-term cycling test were collected, as shown in Fig. S17. The elemental mapping results are in good

agreement with the XPS analysis, confirming that the charged cathode contains considerable S but trace amount of Zn. The S signal could be from the inserted  $\text{SO}_4^{2-}$  in poly(1,5-NAPD) at charged state. In Fig. 6f, broken glass fibers from the separator membrane were embedded in the Zn foil anode. This is because Zn atoms were repeatedly stripped off and plated onto the Zn surface in the cycling process. It should be addressed that, when the cathode and anode were cycled in a beaker-based cell with electrolyte exposed to air, more and larger inorganic flakes would be grown out over their surfaces, evidenced by our SEM (Figs. S18 and S20) and XPS (Fig. S21) measurements. We speculate that the dissolved oxygen in  $\text{ZnSO}_4$  electrolyte, which favors the generation of  $\text{OH}^-$ , promotes the growth of  $\text{Zn}_4(\text{OH})_6\text{SO}_4 \bullet 5\text{H}_2\text{O}$  flakes.

To check the influence of nanoflake byproduct over Zn anode on the cycling performance, we assembled a beaker-based cell (Fig. S22b). After being charged and discharged over  $\sim 1400$  cycles, the Zn foil anode was replaced by a new one. After resuming the cycling test, the capacity was abruptly bounced to a level about 109% of the initial value (Fig. S22a). This indicates that, when in a beaker-based cell with excessive electrolyte, the formation of a large quantity of  $\text{Zn}_4(\text{OH})_6\text{SO}_4 \bullet 5\text{H}_2\text{O}$  flakes over the Zn anode surface is partially responsible for the capacity decay of the cell. The morphology of poly(1,5-NAPD) nanorods in the cathode remained rather stable after a long-term cycling process, as shown in the SEM images in Fig. S23. This could be a reason behind its superb cycling stability.

### 3.6. Factors behind the superb cycling stability of Poly(1,5-NAPD)/AC cathode

Knowing that both poly(1,5-NAPD) and PANI are amino-containing aromatics but PANI shows poor cycling stability when used in pseudocapacitors or Zn-organic batteries [43,44], the long cycling life of the poly(1,5-NAPD) cathode is unlikely to be related to the bond energy change involved in the redox reaction process. It is conceivable that molecular chains in a polymer are randomly oriented and curly. We speculate that the capacity decay of a redox-active polymer is a result of the deficient extraction of ions from the entangled molecular chains during the charging/discharging process. That is, near the outer surface, the polymer provides numerous tunnels among entangled chains to allow ions insertion and desorption. An inserted ion stuck among molecular chains will block its path for other ions diffusion in the following cycling process, causing the capacity decay. Hence, for a cycled polymer electrode, the more trapped  $\text{Zn}^{2+}$  or  $\text{SO}_4^{2-}$  ions inside the polymer, the more capacity loss. To verify this speculation, we tested two poly(1,5-NAPD)/AC cathodes for 500 and 2500 cycles, achieving capacity retentions of 95% and 90%, respectively. To achieve a lower retention, a poly(1,5-NAPD)/CC cathode made by directly electrodepositing poly(1,5-NAPD) onto a bare carbon cloth was tested at  $1 \text{ A g}^{-1}$  for 500 cycles and its capacity retention was 77.5% (Figs. S24 and S25a). The three cycled cathodes were washed by using diluted HCl solution to remove  $\text{Zn}_4(\text{OH})_6\text{SO}_4 \bullet 5\text{H}_2\text{O}$  flakes, and then thoroughly washed by using deionized water. The subsequent XPS analysis for elemental contents, as shown in Fig. S25b and Table S3, is in good agreement with our speculation.

The 3D molecular structures of poly(1,5-NAPD) and PANI are compared in Fig. S26. A poly(1,5-NAPD) molecule at relaxation resembles a helix, while that of PANI is curly and irregular in shape. Presumably, the helix-shaped poly(1,5-NAPD) chains tend to be bundled up during the electrodeposition process, facilitating the growth of nanorods. Among the aligned molecular helices, ions have ample spaces to be efficiently inserted or extracted and their probabilities of being trapped among molecular chains are reduced. Compared to the coating of poly(1,5-NAPD)/AC over a carbon fabric, the carbon-felt-based cathode is more like a pseudocapacitor electrode, as the b-value is higher, and has higher capacity retention after 10000 cycles. Since it has less ion-intercalation reaction but more interfacial pseudocapacitance reaction,

the probability of ions stuck inside the polymer is greatly reduced, accounting for its superb cycling stability.

#### 4. Conclusion

In summary, we devised aqueous rechargeable ZIBs by using a novel cathode material prepared by electrodepositing poly(1,5-NAPD) nanorod arrays onto nanoporous AC granules. The Zn//poly(1,5-NAPD)/AC cell shows gravimetric energy density comparable to that of Li-ion battery, supercapacitor-like high power capability, and long life over 10000 cycles. Two types of current collectors, the flexible carbon cloth and the carbon fiber felt, were used to make ZIBs of different types. With using the flexible carbon fabric, flat pouch or cable-shaped devices were made and showed stable performances when repeatedly bent at large angles. The mass loading of poly(1,5-NAPD)/AC over a carbon fabric can be controlled within a wide range from 2 to 20 mg cm<sup>-2</sup>, rendering energy densities up to 200 Wh kg<sup>-1</sup> or 3.2 mWh cm<sup>-2</sup>. With using the thick carbon felt that can support more cathode material, we demonstrated ZIBs with high specific energy of 7.7 mWh cm<sup>-2</sup>, promising for grid energy storage. The high power capability of our aqueous ZIBs is attributed to the dominant pseudocapacitive behavior of our cathode material. Two button-type ZIBs, with the poly(1,5-NAPD)/AC composite supported by carbon fabric and carbon felt, showed capacity retentions of 91% and 100% after 10000 cycles, respectively. We conclude that Zn<sup>2+</sup>, H<sup>+</sup>, and SO<sub>4</sub><sup>2-</sup> participate in the redox reactions with poly(1,5-NAPD) for charge storage. We found that trapped Zn<sup>2+</sup> and SO<sub>4</sub><sup>2-</sup> in cycled poly(1,5-NAPD) play a key role in reducing the capacity. The superb cycling stability of our ZIB could be related to the helix-structured molecule chains of poly(1,5-NAPD) that not only facilitate the formation of nanorods but also provide unhindered paths among chains for the back-and-forth diffusion of ions in the cycling process.

#### Declaration of competing interest

The authors declare that they have no known competing financial interests or personal relationships that could have appeared to influence the work reported in this paper.

#### CRediT authorship contribution statement

**Yi Zhao:** Investigation, Formal analysis, Writing - original draft. **Yinong Wang:** Formal analysis. **Zhiming Zhao:** Formal analysis. **Jingwen Zhao:** Formal analysis. **Tuo Xin:** Formal analysis. **Na Wang:** Formal analysis. **Jinzhong Liu:** Supervision, Conceptualization, Methodology, Writing - review & editing.

#### Acknowledgements

This work was supported by "The Fundamental Research Funds for Central Universities through Beihang University and The Academic Excellence Foundation of BUAA for PhD students.

#### Appendix A. Supplementary data

Supplementary data to this article can be found online at <https://doi.org/10.1016/j.ensm.2020.03.001>.

#### References

- [1] X. Dong, L. Chen, J. Liu, S. Haller, Y. Wang, Y. Xia, *Sci. Adv.* 2 (2016) e1501038.
- [2] B. Li, Z. Nie, M. Vijayakumar, G. Li, J. Liu, V. Sprenkle, W. Wang, *Nat. Commun.* 6 (2015) 6303.
- [3] R. Wang, Y. Han, Z. Wang, J. Jiang, Y. Tong, X. Lu, *Adv. Funct. Mater.* 28 (2018) 1802157.
- [4] C. Xie, Y. Duan, W. Xu, H. Zhang, X. Li, *Angew. Chem. Int. Ed.* 56 (2017) 14953.
- [5] D. Larcher, J.-M. Tarascon, *Nat. Chem.* 7 (2015) 19.
- [6] D. Selvakumaran, A. Pan, S. Liang, G. Cao, *J. Mater. Chem. A* 7 (2019) 18209.
- [7] M. Mao, T. Gao, S. Hou, C. Wang, *Chem. Soc. Rev.* 47 (2018) 8804.
- [8] Z.A. Zafar, S. Imtiaz, R. Razaq, S. Ji, T. Huang, Z. Zhang, Y. Huang, J.A. Anderson, *J. Mater. Chem. A* 5 (2017) 5646.
- [9] K. Wippermann, J.W. Schultze, R. Kessel, J. Penninger, *Corrosion Sci.* 32 (1991) 205.
- [10] X. Zeng, J. Hao, Z. Wang, J. Mao, Z. Guo, *Energy Storage Mater* 20 (2019) 410.
- [11] Z. Zhao, J. Zhao, Z. Hu, J. Li, J. Li, Y. Zhang, C. Wang, G. Cui, *Energy Environ. Sci.* 12 (2019) 1938.
- [12] L. Kang, M. Cui, F. Jiang, Y. Gao, H. Luo, J. Liu, W. Liang, C. Zhi, *Adv. Energy Mater.* 8 (2018) 1801090.
- [13] W. Sun, F. Wang, S. Hou, C. Yang, X. Fan, Z. Ma, T. Gao, F. Han, R. Hu, M. Zhu, C. Wang, *J. Am. Chem. Soc.* 139 (2017) 9775.
- [14] D. Kundu, B.D. Adams, V. Duffort, S.H. Vajargah, L.F. Nazar, *Nat. Energy* 1 (2016) 1.
- [15] M. Li, Q. He, Z. Li, Q. Li, Y. Zhang, J. Meng, X. Liu, S. Li, B. Wu, L. Chen, Z. Liu, W. Luo, C. Han, L. Mai, *Adv. Energy Mater.* 9 (2019) 1901469.
- [16] J. Ding, Z. Du, L. Gu, B. Li, L. Wang, S. Wang, Y. Gong, S. Yang, *Adv. Mater.* 30 (2018) 1800762.
- [17] T.B. Schon, B.T. McAllister, P.F. Li, D.S. Seferos, *Chem. Soc. Rev.* 45 (2016) 6345.
- [18] F. Wan, L. Zhang, X. Wang, S. Bi, Z. Niu, J. Chen, *Adv. Funct. Mater.* 28 (2018) 1804975.
- [19] H.Y. Shi, Y.J. Ye, K. Liu, Y. Song, X. Sun, *Angew. Chem. Int. Ed.* 57 (2018) 16359.
- [20] J. Wang, J. Liu, M. Hu, J. Zeng, Y. Mu, Y. Guo, J. Wu, X. Ma, Y. Qiu, Y. Huang, *J. Mater. Chem. A* 6 (2018) 11113.
- [21] N. Wang, T. Xin, Y. Zhao, Q. Li, M. Hu, J. Liu, *ACS Sustain. Chem. Eng.* 7 (2019) 14195.
- [22] Y. Liang, Y. Yao, *Joule* 2 (2018) 1.
- [23] X. Yu, A. Manthiram, *ACS Appl. Energy Mater.* 1 (2018) 273.
- [24] S. Betelu, I. Tjijunelyte, L. Boubekeur-Lecaque, I. Ignatiadis, A.C. Schnepf, E. Guenin, N. Bouchehal, N. Felidj, E. Rinnert, M. Lamy de la Chapelle, *J. Org. Inorg. Chem.* 3 (2017) 1.
- [25] R.S. Periatthai, K. Rajagopal, *IOSR J. Appl. Phys.* 6 (2014) 9.
- [26] I. Šeděnková, M. Trchová, J. Stejskal, *Polym. Degrad. Stabil.* 93 (2008) 2147.
- [27] G.M. Brown, G.A. Hope, *J. Electroanal. Chem.* 382 (1995) 179.
- [28] S. Higashi, S.W. Lee, J.S. Lee, K. Takechi, Y. Cui, *Nat. Commun.* 7 (2016) 11801.
- [29] H.L. Girard, H. Wang, A. d'Entremont, L. Pilon, *J. Phys. Chem. C* 119 (2015) 11349.
- [30] V. Augustyn, J. Come, M.A. Lowe, J.W. Kim, P.L. Taberna, S.H. Tolbert, H.D. Abruña, P. Simon, B. Dunn, *Nat. Mater.* 12 (2013) 518.
- [31] D. Chao, C. Zhu, P. Yang, X. Xia, J. Liu, J. Wang, X. Fan, S.V. Savilov, J. Lin, H.J. Fan, Z.X. Shen, *Nat. Commun.* 7 (2016) 12122.
- [32] X. Zhao, B.M. Sánchez, P.J. Dobson, P.S. Grant, *Nanoscale* 3 (2011) 839.
- [33] K. Ghanbari, M.F. Mousavi, M. Shamsipur, H. Karami, *J. Power Sources* 170 (2007) 513.
- [34] Z. Guo, Y. Ma, X. Dong, J. Huang, Y. Wang, Y. Xia, *Angew. Chem. Int. Ed.* 57 (2018) 11737.
- [35] Y. Gogotsi, R.M. Penner, *ACS Nano* 12 (2018) 2081.
- [36] M. Song, H. Tan, D. Chao, H.J. Fan, *Adv. Funct. Mater.* 28 (2018) 1802564.
- [37] L. Zhang, L. Chen, X. Zhou, Z. Liu, *Adv. Energy Mater.* 5 (2015) 1400930.
- [38] G. Sun, X. Jin, H. Yang, J. Gao, L. Qu, *J. Mater. Chem. A* 6 (2018) 10926.
- [39] L. Dong, X. Ma, Y. Li, L. Zhao, W. Liu, J. Cheng, C. Xu, B. Li, Q.H. Yang, F. Kang, *Energy Storage Mater* 13 (2018) 96.
- [40] X. Ma, J. Cheng, L. Dong, W. Liu, J. Mou, L. Zhao, J. Wang, D. Ren, J. Wu, C. Xu, F. Kang, *Energy Storage Mater* 20 (2019) 335.
- [41] R. Salcedo, M. Salmón, M. Aguilar, T. Hernández-Pérez, M. Saloma, *Polymer* 42 (2001) 8737.
- [42] R. Mrówczyński, L. Magerusan, R. Turcu, J. Liebscher, *Polym. Chem.* 5 (2014) 6593.
- [43] A. Eftekhari, L. Li, Y. Yang, *J. Power Sources* 347 (2017) 86.
- [44] C. Kim, B.Y. Ahn, T.S. Wei, Y. Jo, S. Jeong, Y. Choi, I.D. Kim, J.A. Lewis, *ACS Nano* 12 (2018) 11838.